Chinese Chemical Letters 37 (2026) 111568

Contents lists available at ScienceDirect

Chinese Chemical Letters

journal homepage: www.elsevier.com/locate/cclet

Synergistic phenol degradation *via* electron beam irradiation and bimetallic catalysis: Coupling radical and non-radical pathways

Yalan Deng[a], Yaqi Wu[b], Haipeng Xiao[a], Nuowen Ma[a], Huifang Miao[a,c,*], Liuxuan Cao[a,c,*], Wei Guo[d]

[a] College of Energy, Xiamen University, Xiamen 361005, China
[b] College of Chemistry and Chemical Engineering, Xiamen University, Xiamen 361005, China
[c] Fujian Research Center for Nuclear Engineering, Xiamen 361005, China
[d] Biosafety Research Center Yangtze River Delta in Zhangjiagang, Zhangjiagang 215611, China

ARTICLE INFO

Article history:
Received 6 June 2025
Revised 24 June 2025
Accepted 28 June 2025
Available online 18 September 2025

Keywords:
Electron beam irradiation
Copper/cobalt bimetallic catalyst
Radical/non-radical pathway coupling
Phenol irradiation degradation
Coal chemical wastewater treatment

ABSTRACT

Electron beam (EB) irradiation has gained significant attention in industrial wastewater due to its high efficiency and absence of chemical additives or secondary waste. However, its application remains constrained by relatively high operational costs. To address this limitation, we develop a sustainable advanced oxidation platform by synergistically integrating EB irradiation with a bimetallic catalyst ($Cu_{0.97}Co_{0.03}$/AC) for enhanced phenol (Ph) degradation. The Cu-Co bimetallic catalyst activated a dual reaction network encompassing both radical ($^{\bullet}OH$, $^{\bullet}O_2^-$) and non-radical ($^1O_2$, h^+, e^-) pathways, enabling effective Ph degradation. Compared to EB irradiation alone, this integrated system achieved 6.92-fold and 41.43-fold enhancements in Ph degradation and total organic carbon (TOC) removal, respectively. Quenching and trapping experiments confirmed $^1O_2$ and $^{\bullet}OH$ as the dominant reactive species. The system demonstrated broad pH adaptability while avoiding sulfate byproduct formation typically associated with $^1O_2$-based processes. Toxicity assessment confirmed substantial reduction in intermediate toxicity. Meanwhile, the catalyst maintained excellent cycling stability under prolonged irradiation. This work presents a novel approach for efficient degradation and mineralization of highly toxic organic pollutants through radical/non-radical pathway coupling enabled by EB-bimetallic synergy.

© 2026 Published by Elsevier B.V. on behalf of Chinese Chemical Society and Institute of Materia Medica, Chinese Academy of Medical Sciences.

The rapid expansion of the coal chemical industry, driven by growing market demands and technological innovations, has been accompanied by significant environmental challenges due to wastewater generation. Typical coal chemical wastewater contains refractory organic pollutants, including phenolic compounds (*e.g.*, phenol, catechol, and pyrogallol) and polycyclic aromatic hydrocarbons (PAHs; *e.g.*, naphthalene and biphenyl) [1]. These contaminants exhibit persistent biodegradation resistance and have been classified as priority pollutants by regulatory agencies due to their well-documented carcinogenic, teratogenic, and mutagenic properties [2,3]. Phenol (Ph) is one of the most typical organic pollutants generated in coal chemical wastewater, also originates from the production processes of industries such as textile, dyeing, and pharmaceutical industries [4], has garnered particular environmental concerns due to its high toxicity and widespread occurrence. Although the advanced oxidation processes (AOPs), such as Fenton reaction [5,6], ozonation [7–9], persulfate activation [10,11], photocatalytic [12,13], and electrochemical oxidation [14], have shown potential for phenolic compound degradation. Their practical application efficiency is limited by several factors including strict reaction conditions like specific pH and temperature requirements in Fenton reaction, along with the risk from secondary pollution due to the residual oxidants or transformation products, and the extremely short lifespan ($<10^{-6}$ s) and diffusion limitations of the primary reactive oxygen species like hydroxyl radicals ($^{\bullet}OH$), despite their high oxidation potential (2.8 V) [15].

In contrast, ionizing radiation technologies such as electron beam (EB) irradiation offer distinct advantages for wastewater treatment. The radiolysis of water simultaneously generates multiple reactive species, such as hydroxyl radicals $^{\bullet}OH$, hydrated electrons (e_{aq}^-), and hydrogen atoms ($H^{\bullet}$). This process demonstrates unique advantages including chemical-free residuals, and excellent environmental compatibility [16]. The overall reaction formula for the radiolysis of liquid water can be expressed as shown in Eq. 1 [17]. The numbers within parentheses represent the radiation

* Corresponding authors at: College of Energy, Xiamen University, Xiamen 361005, China.
E-mail addresses: hfmiao@xmu.edu.cn (H. Miao), caoliuxuan@xmu.edu.cn (L. Cao).

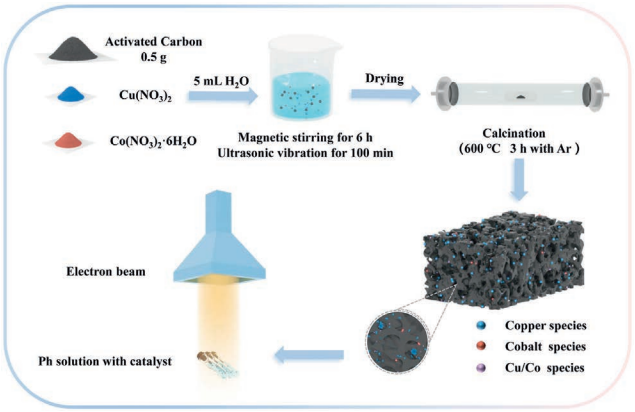
https://doi.org/10.1016/j.cclet.2025.111568
1001-8417/© 2026 Published by Elsevier B.V. on behalf of Chinese Chemical Society and Institute of Materia Medica, Chinese Academy of Medical Sciences.

chemical yield G-values (μmol/J) of each species.

$$H_2O \rightarrow H_2(0.45) + H_2O_2(0.71) + e_{aq}^{-}(2.6) + H^{\bullet}(0.55) + {}^{\bullet}OH(2.7) + H_3O^{+}(2.6) \quad (1)$$

Despite the advantages of ionizing radiation technology, its large-scale application remains constrained by high operational costs, primarily attributed to the accumulation of intermediate byproducts and suboptimal mineralization efficiency. To address these limitations, catalysts or auxiliary reagents are increasingly integrated into ionizing radiation processes to enhance both degradation rate and mineralization efficiency of organic pollutants. For example, Chitose *et al.* used EB to irradiate the Ph solution containing titanium dioxide nanoparticles, greatly accelerating the removal of total organic carbon (TOC) [18]. Alkhuraiji *et al.* utilized ionizing radiation to investigate the degradation and mineralization of Ph and discovered that the combination of O_3, H_2O_2, N_2O, O_2, or $S_2O_8^{2-}$ reagents with ionizing radiation effectively enhances the radioactive degradation system for phenol degradation or mineralization [19]. Current EB-catalysis systems predominantly rely on radical-mediated mechanisms for pollutant degradation [20].

However, studies of non-irradiated catalytic systems reveal that synergistic integration of radical and non-radical pathways can significantly enhance both degradation rate and mineralization efficiency of pH. For instance, some catalysts in AOPs can further generate singlet oxygen ($^1O_2$), a reactive species with distinct advantages. Among various reactive oxygen species, $^1O_2$ (2.2 V) has attracted considerable attention due to its extended lifetime (2×10^{-6} s) [15]. Notably, $^1O_2$ exhibits excellent selectivity and interference resistance while maintaining robust reactivity across a wide pH range. Consequently, non-radical oxidation systems dominated by $^1O_2$ demonstrate promising application prospects for organic pollutant removal, making $^1O_2$-mediated reactions an emerging research focus in AOPs [21]. To achieve efficient and controllable generation of $^1O_2$, researchers have recently turned their attention to biochar (BC)-based transition metal composites. These materials have demonstrated remarkable potential in environmental catalysis owing to their tunable metal active sites, superior electron transfer capability, and porous structures [22,23]. Research indicates that metal doping (*e.g.*, Cu, Fe, Co), heteroatom modification (*e.g.*, N, O), and pyrolysis temperature optimization can effectively enhance the catalytic performance of biochar. For example, Wang *et al.* discovered that Cu-doped cow dung biochar facilitates uniform distribution of iron sites, which accelerated the generation of $^{\bullet}OH$, $^1O_2$, and superoxide radicals ($^{\bullet}O_2^-$) [24]. Similarly, Xi *et al.* demonstrated that Fe@N co-doped biochar could activate persulfate (PS) to degrade 95 % norfloxacin (NOR) through a dual mechanism involving both radical ($^{\bullet}OH/SO_4^{\bullet-}$) and non-radical ($^1O_2$) species [25]. For non-metallic catalysts, Qu *et al.* reported that porous hydrochar (PHC) derived from corn straw could activate PS to generate $^1O_2$ and mediate electron-transfer-dominated phenol degradation [22]. Furthermore, Zhang *et al.* achieved 91.57 % tetracycline hydrochloride (TC) degradation through a $^1O_2$-dominated non-radical pathway by activating peroxymonosulfate (PMS) with *Camellia oleifera* shell-derived biochar (COSB-1000) pyrolyzed at 1000 °C [21]. While these studies demonstrate the feasibility of dual radical/non-radical mechanisms in non-irradiated systems, their potential synergy within irradiation-catalysis systems remains unexplored. The radiolysis of water triggered by ionizing radiation coupled with catalytic systems provides a continuous, chemical-free source of reactive radicals. Existing studies have demonstrated that catalysts containing unsaturated metal sites can significantly facilitate either the rapid conversion of $^{\bullet}OH$ to $^1O_2$ or the direct generation of $^1O_2$ [26]. These evidences suggest that EB-catalysis systems incorporating radical/non-radical oxidation routes may achieve breakthrough improvements in operational efficacy and cost-efficiency. But relevant studies are still absent.



Scheme 1. The schematic of Cu_x/AC ($x = 1$, 2, 3) and $Cu_{1-x}Co_x$/AC ($x = 0.03$, 0.06, 0.09, 0.12) preparation and electron beam irradiation process. The activated carbon was derived from coconut shells. During the synthesis of Cu_x/AC, the copper ion concentration was maintained at 0.675, 1.35, and 2.025 mmol. During the synthesis of $Cu_{1-x}Co_x$/AC, the molar ratios of Cu^{2+} and Co^{2+} were adjusted while maintaining the total metal ion concentration at 0.675 mmol.

In this paper, we report a novel radiation-catalytic strategy that activates a dual reaction network comprising radical and non-radical pathways using bimetallic catalysts ($Cu_{1-x}Co_x$/AC) for efficient Ph degradation. EB irradiation directly generated reactive species ($^{\bullet}OH$, e_{aq}^-, $H^{\bullet}$) for primary pollutant degradation, while the coconut shell-derived activated carbon (AC)-supported bimetallic catalyst, fabricated *via* impregnation with optimized Cu/Co ratios (97:3), effectively catalyzed radiolytically produced H_2O_2, thereby constructing a dual reaction network encompassing both radical ($^{\bullet}OH$, $^{\bullet}O_2^-$) and non-radical ($^1O_2$, h^+, e^-) pathways. The degradation performance was evaluated under varying irradiation doses, catalyst dosages, pH values, and through recycling experiments. In addition, the catalytic mechanism and degradation performance were systematically characterized by HPLC and X-ray photoelectron spectroscopy (XPS). Electron paramagnetic resonance (EPR) analyses were employed to validate the catalytic mechanisms involving both radical and non-radical species formation during Ph oxidation. Finally, the degradation pathways of this system were discussed. The ecological risks of Ph and its degradation intermediates were evaluated using the Toxicity Estimation Software Tool (T.E.S.T). This study established an innovative radiation-catalytic synergy mechanism coupling radical and non-radical pathways, providing a groundbreaking strategy for highly efficient degradation mineralization of recalcitrant organic pollutants.

All materials used in this study are detailed in Text S1 (Supporting information). The materials were prepared according to the steps as shown in Scheme 1. Above all, coconut shell was selected as the raw material and carbonized at 550 °C to obtain activated carbon (AC). The AC was purified through three successive washing cycles with deionized water (18.2 MΩ cm at 25 °C Milli-Q), followed by oven-drying at 100 °C for 12 h. In a typical preparation, AC (0.5 g) and Cu $(NO_3)_2$ (0.675 mmol/1.35 mmol/2.025 mmol) were dissolved in deionized water (5 mL) under magnetic stirring (450 rpm, 6 h), then ultrasonicated for 100 min. The homogeneous mixture was dried at 100 °C for 12 h. Finally, the resulting precursor was calcined in the tube furnace under dynamic vacuum with programmed heating (5 °C/min to 600 °C) under Ar flow (50 sccm), maintained at 600 °C for 3 h, and cooled to room temperature naturally. The obtained catalysts were designated as Cu_1/AC, Cu_2/AC, and Cu_3/AC respectively in this article.

The $Cu_{1-x}Co_x$/AC was prepared in the same manner with the addition of Co $(NO_3)_2 \cdot 6H_2O$. The molar ratios of Cu^{2+} and Co^{2+} were systematically varied while maintaining the total metal ion concentration at 0.675 mmol in the precursor solution.

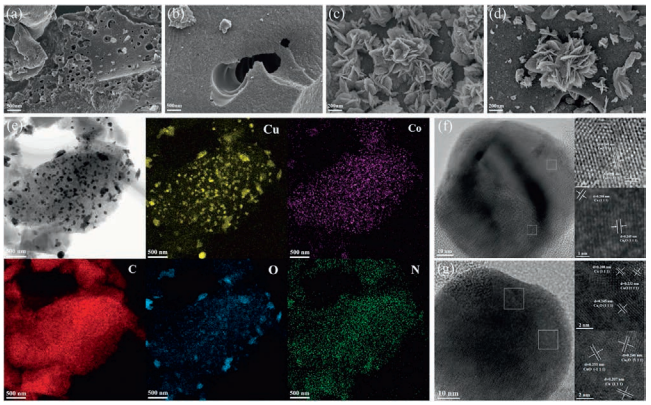


Fig. 1. Morphological characterization of catalysts. (a-d) SEM images of C-AC, AC, Cu_1/AC and $Cu_{0.97}Co_{0.03}$/AC. C-AC exhibited irregular cavities and non-uniform pores. AC displayed wider, interconnected pore channels. Cu_1/AC and $Cu_{0.97}Co_{0.03}$/AC nanocrystals adopted plate-like and spherical morphologies. (e) Elemental mapping of C, O, N, Cu, Co in the $Cu_{0.97}Co_{0.03}$/AC composite. (f, g) TEM images of $Cu_{0.97}Co_{0.03}$/AC. The lattice fringes demonstrated the coexistence of metallic Cu and its oxides.

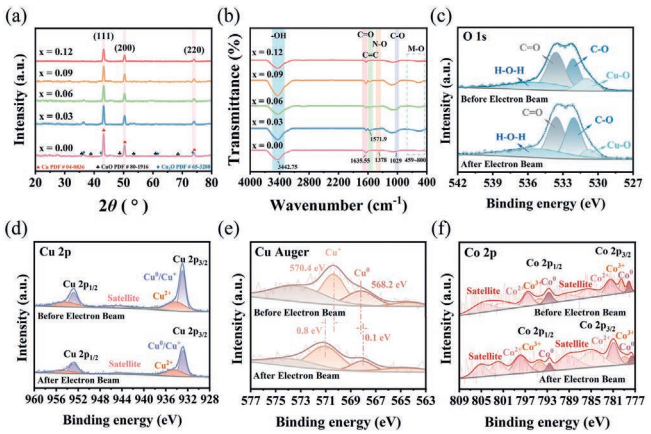


Fig. 2. Structural characterization. (a) XRD spectra of $Cu_{1-x}Co_x$/AC. (b) FT-IR spectra of $Cu_{1-x}Co_x$/AC ($x = 0$, 0.03, 0.06, 0.09 and 0.12). Specific XPS analysis of $Cu_{0.97}Co_{0.03}$/AC before and after EB: (c) O 1s, (d) Cu 2p, (e) Cu Auger and (f) Co 2p.

In this study, Ph was selected as the target contaminant with an initial concentration of 50 mg/L. The adsorption and degradation kinetics were monitored by measuring Ph concentration changes *via* HPLC. In a typical experiment, 5 mg catalyst was dispersed in 10 mL Ph solution and mixed for 6 h. The mixture was then irradiated at room temperature using a 10 MeV, 20 kW electron linear accelerator (model: IS1020). After syringe-filtration (0.22 μm PES membrane), Ph concentration was analyzed by HPLC. With the increasing dose of irradiation, the Ph concentration showed a regular decreasing trend. The relationship between the initial Ph concentration (C_0) and final concentration (C), along with degradation efficiency, could be characterized by Eq. 2. The concentration changes of Ph was found to conform to the reaction kinetic model presented in Eq. 3 [27].

$$\text{Degradation efficiency} = \frac{C_0 - C}{C} * 100\% \quad (2)$$

$$\ln (C_0/C) = kD \quad (3)$$

where D represents the absorbed dose, and k is the degradation rate constant (1/kGy).

The effects of different parameters including irradiation dose (0–3.6 kGy), solution pH (2.65–10.23), and catalyst concentration (0–0.9 g/L) were investigated. All experiments were repeated twice to ensure consistency and reproducibility of the results. The characterization instruments and methods are provided in Supporting information.

Morphology and microstructure of the catalysts were characterized by scanning electron microscope (SEM), transmission electron microscope (TEM), and energy-dispersive spectroscopy (EDS). Figs. 1a-d present SEM images of commercial activated carbon (C-AC), coconut shell activated carbon (AC), Cu_1/AC, and $Cu_{0.97}Co_{0.03}$/AC, respectively. C-AC exhibited irregular cavities and non-uniform pores on its surface (Fig. 1a), whereas AC displayed wider, interconnected pore channels (Fig. 1b), likely formed due to the release of volatile compounds during carbonization. This hierarchical porous structure provided a high surface area (1339 m^2/g), facilitating metal ion loading and enhanced reactant diffusion to improve catalytic efficiency. The $Cu_{1-x}Co_x$/AC ($x = 0$–0.03) nanocrystals adopted plate-like and spherical morphologies, with noticeable aggregation on the AC surface and within pore channels. Notably, Cu_1/AC nanoparticles showed significant agglomeration (Fig. 1c), Co incorporation ($Cu_{0.97}Co_{0.03}$/AC) improved dispersion uniformity and reduced the crystal size (Fig. 1d). After metal loading, the macropores originally present in AC surface disappeared, potentially due to metal nanoparticle pore blockage or structural collapse during calcination.

The porosity characteristics of AC and $Cu_{0.97}Co_{0.03}$/AC were investigated through nitrogen adsorption experiment at 77.3 K. The adsorption-desorption isotherms exhibited a sharp nitrogen uptake at low relative pressure ($P/P_0 = 0$–0.01) followed by a plateau, characteristic of microporous materials (Fig. S1 in Supporting information). Furthermore, the absence of hysteresis in the adsorption-desorption isotherms of $Cu_{0.97}Co_{0.03}$/AC demonstrated its minimal mesoporous character [28]. This adsorption-desorption isotherm is classified as Type I according to the classification of International Union of Pure and Applied Chemistry (IUPAC) [29]. The specific surface area and average pore size of AC and $Cu_{0.97}Co_{0.03}$/AC are summarized in Table S1 (Supporting information). After modification with Cu-Co nanoparticles, the BET surface area increased from 1339 m^2/g to 1581 m^2/g, with a notable rise in micropore surface area (from 885 m^2/g to 1556 m^2/g) while the external surface area significantly decreased from 454 m^2/g to 24.86 m^2/g. This contrast suggests that metal nanoparticles preferentially occupied micropores while potentially blocking larger pores. Furthermore, the total pore volume and micropore volume increased from 0.69 cm^3/g to 0.71 cm^3/g and 0.43 cm^3/g to 0.66 cm^3/g, respectively, while the average pore width decreased from 2.1 nm to 1.79 nm. These structural modifications likely attributed to the uniform dispersion of metal nanoparticles within micropores, calcination-induced pore restructuring through sintering, and partial collapse of pore channels during thermal treatment. These factors synergistically enhance microporosity while reducing larger pores.

As shown in Fig. 1e, TEM imaging with corresponding EDS elemental mapping confirmed the coexistence of C, Cu, Co, O, and N elements in the $Cu_{0.97}Co_{0.03}$/AC composite. The Cu species exhibited a predominantly uniform distribution, although occasional localized aggregation was observed. Only trace oxygen signals were detected by EDS, suggesting negligible surface oxidation. TEM analysis (Figs. 1f and g) identified well-defined lattice fringes with measured spacings of 0.208 nm, 0.245 nm, and 0.255 nm, corresponding to the (111) planes of metallic Cu, Cu_2O, and the (−111) planes of CuO, respectively. These results demonstrated that the nanoparticles consist predominantly of Cu/Cu_2O phases, with trace amounts of CuO.

X-ray diffraction analysis (XRD) analysis was employed to characterize the crystal structure of the synthesized $Cu_{1-x}Co_x$/AC catalysts. As illustrated in Fig. 2a, all samples with different Co doping concentrations displayed similar diffraction patterns. Notably, the

diffraction peak intensities progressively decreased with increasing Co content, which could be ascribed to either crystallite size reduction induced by doping or lattice parameter reduction caused by Co species substitution for Cu species [30]. XRD analysis confirmed the coexistence of metallic Cu, Cu_2O, and CuO phases in the catalysts. The diffraction peaks observed at 43.2°, 50.4°, and 74.1° were assigned to the (111), (200), and (220) crystal planes of Cu (PDF #04–0836), respectively [31]. Notably, $Cu_{0.88}Co_{0.12}$/AC exhibited a positive 0.069° shift in these peaks compared to Cu_1/AC, indicating lattice contraction due to the substitution of Co ions with smaller ionic radius into the original Cu sites, resulting in reduced lattice constants. Additional characteristic peaks at 36.5°, 42.4°, 61.5°, and 73.7° were indexed to the (111), (200), (220), and (311) planes of Cu_2O (PDF #65–3288), whereas peaks at 35.5°, 38.7°, and 48.6° corresponded to the (−111), (111), and (−202) planes of CuO (PDF #80–1916) [30]. Fig. 2b displays the FT-IR spectra of $Cu_{1-x}Co_x$/AC in the 4000–400 cm^{-1} range. The broad absorption band centered at ~3450 cm^{-1} is assigned to the O–H stretching vibration of hydrogen-bonded hydroxyl groups. The characteristic peaks at 1635.6 cm^{-1} and 1571 cm^{-1} correspond to C=O and aromatic C=C stretching vibrations, respectively, while the peak at 1029 cm^{-1} represents C–O stretching [32,33]. The absorption band at 1378 cm^{-1} originates from N–O stretching of surface-adsorbed nitrate species derived from the precursor salts $Co(NO_3)_2 \cdot 6H_2O$ and $Cu(NO_3)_2$. Additionally, the low-wavenumber absorptions (459–800 cm^{-1}) are attributed to M-O (M = Cu, Co) stretching vibrations [34].

To investigate the structural composition and elemental states of $Cu_{0.97}Co_{0.03}$/AC, XPS analyses were performed both before and after irradiation. The survey spectrum (Fig. S2a in Supporting information) confirmed the presence of C, O, Cu, and Co as the primary elements. The C 1s spectrum exhibited four characteristic peaks at 284.8, 285.9, 289.0, and 291.3 eV (Fig. S2b in Supporting information), corresponding to C–C, C–O, C=O functional groups, and π-π interactions, respectively [4,35]. The O 1s spectrum (Fig. 2c) was deconvoluted into four peaks at 531.0 eV (Cu-O), 532.1 eV (C–O), 533.6 eV (C=O), and 535.2 eV (H–O-H). The Cu-O peak confirms the coordination between C–O groups and Cu atoms, while the presence of C–O and H–O–H functional groups enhances the surface hydrophilicity and electrolyte permeability of $Cu_{0.97}Co_{0.03}$/AC [36].

In the Cu 2p spectrum (Fig. 2d), the peaks at 934.2 and 932.9 eV were assigned to Cu^{2+} and Cu^+/Cu^0 species, respectively. The intense shake-up satellite features observed in the range of 939-946 eV (Cu $2p_{3/2}$) further confirmed the presence of Cu^{2+} species [37]. After irradiation, the intensity of the Cu^+/Cu^0 peak decreased, while the Cu^{2+} peak intensified, indicating the occurrence of Cu^+/Cu^0 oxidation to Cu^{2+} during the reaction. Comparative analysis revealed that the Cu^{2+} peaks (Cu $2p_{3/2}$ and Cu $2p_{1/2}$) and their corresponding satellite features in Cu_1/AC (Fig. S2c in Supporting information) exhibited greater intensity enhancement post-irradiation than those in $Cu_{0.97}Co_{0.03}$/AC. This observation demonstrated that Co doping effectively attenuated the irradiation-induced oxidation of Cu^+/Cu^0 to Cu^{2+}, thereby regulating the material's oxidation state.

The Cu LMM Auger spectrum (Fig. 2e) was further analyzed to differentiate Cu^+ and Cu^0 species. The deconvoluted peaks at 568.2 eV and 570.4 eV were assigned to Cu^0 and Cu^+, respectively, while other peaks represent different transition states in the Cu Auger spectrum [38]. Although Cu^{2+} Auger features also appear between 569.0 and 570.0 eV, their minimal intensity confirmed negligible contribution. After irradiation, Cu^0 and Cu^+ peaks in $Cu_{0.97}Co_{0.03}$/AC showed a 0.1 eV negative shift and 0.8 eV positive shift, respectively, whereas the Cu^+ peak in the Cu_1/AC showed only a 0.2 eV negative shift (Fig. S2d in Supporting information). These results demonstrate that Co doping significantly modifies the chemical environment of Cu species. The Auger parameter values around 1849 eV for all samples indicated that copper species in these materials predominantly adopted the characteristic spectral profile of Cu^+(Fig. S3 in Supporting information) [39]. Both the Auger spectrum and Auger parameter analysis consistently demonstrated that Cu^+ represented the dominant copper species in $Cu_{0.97}Co_{0.03}$/AC.

In the Co 2p spectrum (Fig. 2f), the peaks at 778.1 and 792.7 eV were assigned to Co $2p_{3/2}$ and Co $2p_{1/2}$ of Co^0, respectively [40,41]. The Co $2p_{3/2}$ main peak exhibited asymmetric with weak satellite features. The sharper and more intense component at lower binding energy corresponded to Co^{3+}, while the higher binding energy component represented Co^{2+} species. In the Co $2p_{3/2}$ spectral region of the composite sample, the deconvoluted peaks centered at 779.4 and 781.4 eV were assigned to Co^{3+} and Co^{2+}, respectively [42]. Similarly, in the Co $2p_{1/2}$ region, the fitted peaks at 794.4 and 796.6 eV were identified as Co^{3+} and Co^{2+} components, correspondingly.

Owing to the multiple advantages of copper-based catalysts, including low cost, superior catalytic performance, environmental compatibility, wide applicability, and sustainability, copper species were selected as the primary dopant in this study. To optimize the metal doping ratio for achieving enhanced radiation-catalytic degradation, a series of Cu_x/AC catalysts ($x = 1$–3) were synthesized through impregnation with gradient molar quantities of $Cu(NO_3)_2$. Their Ph degradation efficiencies were quantitatively assessed using C-AC and AC as reference materials. The results are presented in Fig. 3a. Among the tested catalysts, Cu_1/AC demonstrated superior catalytic performance, increasing the Ph removal rate from 27.49 % (EB alone) to 83.32 % at 1 kGy, corresponding to a 35 % improvement over C-AC. Intriguingly, C-AC displayed a relatively low kinetic constant ($k = 0.495$), comparable to that of EB irradiation alone ($k = 0.322$), presumably due to its pronounced adsorption capacity. By contrast, the k-value of AC and Cu_1/AC reached 1.253 and 1.467, respectively. However, elevated metal loading adversely affected both Ph removal efficiency and k-values, demonstrating that excessive metal loading does not generate additional active sites but rather causes site blocking. Thus, the ideal metal loading of 0.675 mmol was determined for subsequent studies.

To identify optimal metal elements for enhancing radiation-catalytic degradation, we investigated the Ph degradation performance of bimetallic catalysts with varying metal combinations (Cu/Co, Cu/Fe, Cu/Mn, and Cu/Ni). As shown in Fig. 3b, all tested combinations exhibited Cu^{2+} leaching concentrations below the permissible limit specified in the Environmental Quality Standards for Surface Water (GB 3838–2002; Cu^{2+} concentration: 1.0 mg/L). Notably, the Cu/Co bimetallic system demonstrated not only the highest degradation performance but also the lowest Cu^{2+} leaching rate (<0.2 mg/L).

We also synthesized a series of bimetallic $Cu_{1-x}Co_x$/AC catalysts ($x = 0.03$, 0.06, 0.09, 0.12) and evaluated their Ph degradation efficiency. Kinetic analysis revealed that most Cu/Co catalysts exhibited higher k-values than Cu_1/AC (Fig. S4 in Supporting information), demonstrating distinct synergy between the two metals. Both phenol degradation efficiency and k-value reached a maximum at 3 at % cobalt doping (Fig. 3c), beyond which higher Co loading led to decreased reaction rates and removal efficiency. Thus, $Cu_{0.97}Co_{0.03}$/AC was identified as the optimal catalyst and selected for further studies.

Fig. 3d presents the adsorption and degradation curves of Ph in the $Cu_{0.97}Co_{0.03}$/AC-EB system, reflecting the variation of Ph concentration with increasing irradiation dose. At a dose of 0.5 kGy, $Cu_{0.97}Co_{0.03}$/AC exhibited remarkably enhanced catalytic activity for Ph degradation compared to C-AC, achieving removal rates of 82.2 % and 45.4 %, respectively, whereas EB alone resulted in only 14.3 % removal. The pronounced degradation of Ph observed in the initial stage is attributed to the rapid generation of reactive radicals that drive the oxidative degradation process. Nevertheless,

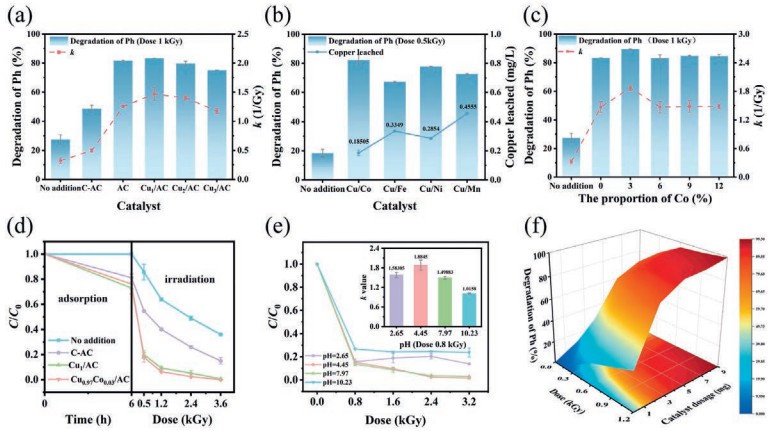


Fig. 3. Irradiation degradation performance of catalysts. (a) Degradation rate and reaction rate constant (*k*-value) of different catalysts at 1 kGy. (b) Ph degradation rate and copper leaching levels for catalysts with different metal compositions at 0.5 kGy. (c) Influence of cobalt ratios on Ph degradation at 1 kGy. (d) Effect of radiation dose on Ph removal. (e) Effect of Ph values on Ph removal. (f) Effect of catalyst dosage on Ph removal. Experiment conditions: initial Ph concentration = 50 mg/L, catalysts dosage = 0.5 g/L.

the removal efficiency decreased gradually with prolonged reaction time, likely due to the accumulation of intermediate byproducts that both scavenge reactive radicals and compete with Ph for active sites.

To evaluate the practical application of wastewater treatment across a wide pH range, we investigated the catalytic performance under different pH conditions. As depicted in Fig. 3e, the original Ph solution was weakly acidic, with a pH of 4.45. The pH was subsequently adjusted to 2.65 (acidic), 7.97 (near-neutral), and 10.23 (alkaline) using HCl or NaOH, respectively. While the Ph removal efficiencies were comparable under near-neutral conditions and at the natural pH, the *k*-value at 0.8 kGy decreased from 1.88 to 1.50 as the pH increased from 4.45 to 7.97. However, under alkaline conditions, the Ph degradation efficiency dropped significantly, reaching a maximum removal rate of only 77 %. The *k*-value for radiation degradation sharply decreased to 1.02. ICP-MS analyses confirmed negligible metal ion leaching (Fig. S5 in Supporting information), ruling out the influence of dissolved metal species. The decrease in catalytic activity may be attributed to a dual deactivation mechanism: the formation of metal hydroxide complexes at high pH induce surface passivation by physically blocking catalytic active sites [32], while the alkaline environment inhibited Ph degradation by consuming $^{\bullet}OH$ through their reaction with OH^-, as illustrated in Eq. 4 [43]. These results demonstrate the crucial role of $^{\bullet}OH$ radicals in the catalytic degradation process.

$$^{\bullet}OH + OH^- \rightarrow {}^{\bullet}O^- + H_2O \quad (4)$$

The effect of $Cu_{0.97}Co_{0.03}$/AC dosage (0–0.9 g/L) on Ph removal efficiency is shown in Fig. 3f. As the catalyst dosage increased from 0 to 0.5 g/L, the Ph removal efficiency at 1.2 kGy improved remarkably from 36.1 % to 94.2 %. This enhancement can be attributed to the increased number of active sites with higher $Cu_{0.97}Co_{0.03}$/AC dosage, which promotes Ph degradation. However, further increasing the dosage to 0.7 and 0.9 g/L resulted in only marginal improvements of 1.75 % and 5.23 %, respectively. These results indicate that higher dosages of $Cu_{0.97}Co_{0.03}$/AC do not significantly influence the degradation efficiency of Ph.

To independently assess the contributions of adsorption and degradation by $Cu_{0.97}Co_{0.03}$/AC to Ph removal, nonlinear fitting was performed on the adsorption data using four kinetic models: The *pseudo*-first-order kinetic model as described in Eq. S1 (Supporting information), the *pseudo*-second-order kinetic model in Eq. S2 (Supporting information), the Elovich model in Eq. S3 (Supporting information), and the Bangham kinetic model in Eq. S4 (Supporting information). The intraparticle diffusion behavior of Ph within the catalyst was further analyzed using the Weber-Morris model according to Eq. S5 (Supporting information) [44–47]. The fitting results are presented in Fig. S6 (Supporting information), and the corresponding parameters for the four models are listed in Table S2 (Supporting information).

As shown in Figs. S6a-d (Supporting information), the Bangham model demonstrated the best fit ($R^2 = 0.969$) among all kinetic models, indicating that Ph adsorption on $Cu_{0.97}Co_{0.03}$/AC followed a pore-diffusion-controlled mechanism. Initially, phenol molecules occupied the active sites on the catalyst surface. Upon saturation of these surface sites, the molecules subsequently diffused into the internal porous structure and occupied adsorption sites within the pore. The fitted curve of the Weber-Morris model is presented in Fig. S6e (Supporting information). The adsorption process of Ph on $Cu_{0.97}Co_{0.03}$/AC can be clearly divided into three stages based on the slope variations of the kinetic curve. The initial stage involved external surface diffusion of phenol molecules, where larger specific surface area of the catalyst provided more available adsorption sites, resulting in higher k_1 values. When the surface sites became saturated, the process transitioned to intraparticle diffusion into the pore structure, during which catalysts with higher microporosity demonstrated stronger adsorption capacity. The final equilibrium stage occurred when the adsorption sites within the micropores became fully occupied, leading phenol molecules to adsorb onto the mesoporous structures that originally served as transport channels. Therefore, both the specific surface area and pore structure of $Cu_{0.97}Co_{0.03}$/AC were found to significantly influence its Ph adsorption performance. The adsorption experiments revealed an optimal adsorption time of 6 h for this catalyst. The degradation efficiency can be calculated by subtracting the adsorption quantity from the total removal quantity.

Catalytic degradation of organic pollutants generally proceeds through both free-radical and non-free-radical pathways. To identify the dominant reactive oxygen species (ROS) in the $Cu_{0.97}Co_{0.03}$/AC-EB system, quenching experiments and EPR analysis were performed.

As shown in Fig. 4a, the addition of 0.1 mol/L TBA reduced the *k*-value of Ph degradation from 1.73 to 0.44 at 1.2 kGy, corresponding to a 39.3 % decrease in removal efficiency. Under the same irradiation conditions, 0.01 mol/L-His decreased Ph removal by 44 %, with this inhibitory effect intensifying at a higher L-His concentration of 0.1 mol/L (54.1 % inhibition at maximum; Fig. 4b). These results confirmed that $^1O_2$ played a critical role in Ph degradation. Given that $^1O_2$ exhibits a significantly longer lifetime in D_2O (30–32 μs) than in H_2O (2 μs), theoretical analysis predicted that Ph

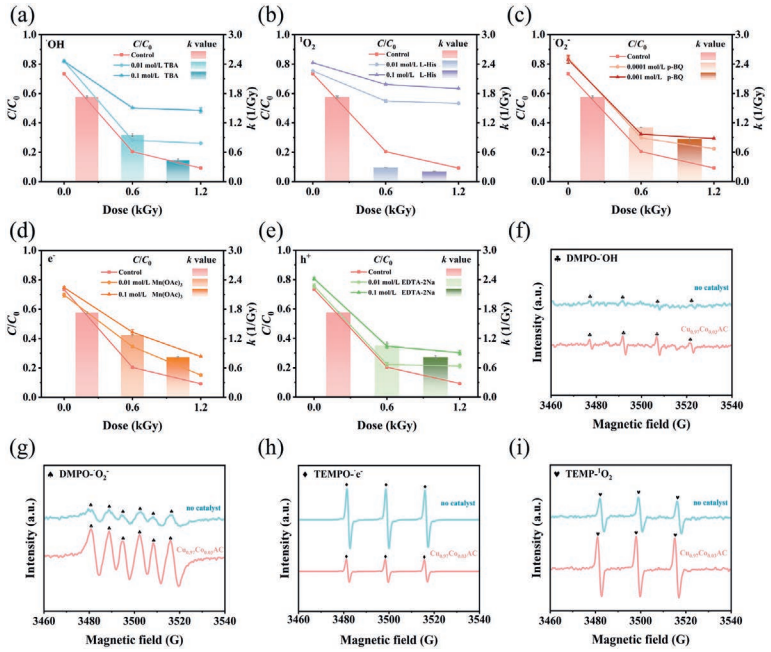
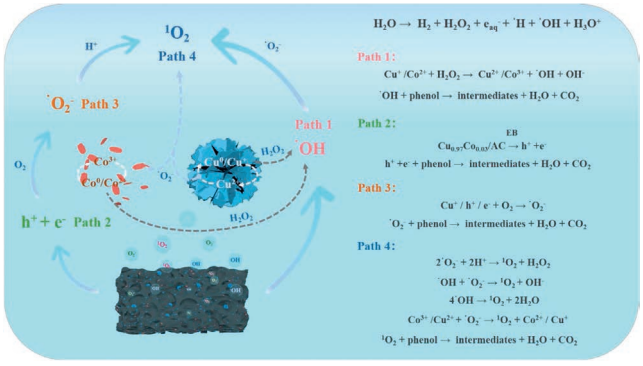


Fig. 4. Radical scavenging effects on Ph degradation and EPR analysis. Ph degradation rate with addition of (a) TBA, (b) L-His, (c) *p*-BQ, (d) $Mn(OAc)_3$ and (e) EDTA-2Na. Scavenger concentration: 0.0001–0.1 mol/L. EPR spectra of the $Cu_{0.97}Co_{0.03}$/AC-EB system: (f) DMPO adduct in deionized water, (g) DMPO adduct in methanol, (h) TEMPO adduct in Ph solution and (i) TEMP adduct in 20 wt% D_2O solution. Experiment conditions: Ph = 50 mg/L, $Cu_{0.97}Co_{0.03}$/AC = 0.5 g/L.

degradation would be faster in D_2O if $^1O_2$ participated in the reaction [48,49]. To further verify $^1O_2$ generation, D_2O was substituted for H_2O as the reaction solvent. Notably, Ph degraded faster in D_2O than in H_2O, providing conclusive evidence for $^1O_2$ production in the $Cu_{0.97}Co_{0.03}$/AC-EB system (Fig. S7 in Supporting information). The addition of 0.0001 mol/L and 0.001 mol/L *p*-BQ significantly inhibited Ph removal at 1.2 kGy, with degradation rates decreasing to 77.67 % and 70.74 %, respectively (Fig. 4c). This inhibition confirmed substantial $^{\bullet}O_2^-$ production in the system. In contrast, $Mn(OAc)_3$ and EDTA-2Na exhibited minimal quenching effects. Even at the higher concentration of 0.1 mol/L, Ph removal rates were only reduced by 18.6 % and 21 % respectively (Figs. 4d and e). These results demonstrated that although electron transfer occurred during the reaction process, the direct contribution of e^- and h^+ to the oxidative reaction was limited. The quenching experiments confirmed that the system contained $^{\bullet}OH$, $^{\bullet}O_2^-$, $^1O_2$, h^+, and e^-, where $^{\bullet}OH$ and $^1O_2$ acted as the dominant reactive species in the degradation process.

EPR spectroscopy was employed to verify the corresponding ROS in different systems. Strong signals of $^{\bullet}O_2^-$, e^-, and $^1O_2$ were observed in the $Cu_{0.97}Co_{0.03}$/AC-EB system (Figs. 4g-i), while the $^{\bullet}OH$ signal intensity was significantly weaker (Fig. 4f). This phenomenon can be attributed to the strong adsorption of $^{\bullet}OH$ on the $Cu_{0.97}Co_{0.03}$/AC surface, while DMPO primarily captured $^{\bullet}OH$ in the solution [15]. Furthermore, the high specific surface area and porous structure of $Cu_{0.97}Co_{0.03}$/AC provided abundant active sites for continuous recombination of $^{\bullet}OH$ and $^{\bullet}O_2^-$ into $^1O_2$. This process enhanced $^1O_2$ production while consequently reducing the $^{\bullet}OH$ signal detectable by DMPO. Notably, while the EPR signal (Fig. 4h) confirms e^- production, the quenching data conclusively show these e^- function indirectly, primarily mediating ROS generation rather than directly attacking Ph.

To elucidate the catalytic mechanism, we analyzed the changes of elemental valence states and potential radical reactions. Radical quenching and trapping experiments confirmed the existence of h^+ and e^- in the $Cu_{0.97}Co_{0.03}$/AC-EB system (Eq. 5). Previous studies have demonstrated that H_2O_2 generated during water radiolysis



Scheme 2. Radical ($^{\bullet}OH$, $^{\bullet}O_2^-$) and non-radical ($^1O_2$, h^+, e^-) oxidation mechanism for Ph degradation in the $Cu_{0.97}Co_{0.03}$/AC-EB system. $^{\bullet}OH$ and $^1O_2$, acted as the dominant reactive species in the degradation process. $^{\bullet}O_2^-$ served as a crucial intermediate for both H_2O_2 production and $^1O_2$ formation.

participated in Fenton-like reactions with Cu/Co species (Eqs. 6–9). Critically, the $^{\bullet}OH$ generated by radiation served as transient intermediates that generated $^{\bullet}O_2^-$ and $^1O_2$. Cu^0 reacted with $^{\bullet}OH$ to form Cu^+ (Eq. 10). These Cu^+ ions, along with h^+ and e^-, directly reacted with dissolved oxygen to produce $^{\bullet}O_2^-$ (Eqs. 11–13). $^1O_2$ was generated through both disproportionation and Haber-Weiss reactions between radicals (Eqs. 14–16). Notably, Co^{3+} and Cu^{2+} further enhanced the conversion of $^{\bullet}O_2^-$ to $^1O_2$ (Eqs. 17 and 18), while the Co species facilitated the valence cycling of copper (Eq. 19). Furthermore, $^{\bullet}O_2^-$ generated H_2O_2 *via* single-electron transfer, which led to H_2O_2 accumulation and sustained Fenton-like reactions (Eq. 20). $^{\bullet}O_2^-$ served as a crucial intermediate for both H_2O_2 production and $^1O_2$ formation. The integrated mechanism is schematically summarized in Scheme 2 [26,50].

$$Cu_{0.97}Co_{0.03}/AC \xrightarrow{EB} h^+ + e^- \quad (5)$$

$$2Cu^0 + H_2O_2 \rightarrow 2Cu^+ + 2OH^- \quad (6)$$

$$Cu^{+} + H_2O_2 \rightarrow Cu^{2+} + {}^{\bullet}OH + OH^{-} \quad (7)$$

$$Co^{0} + H_2O_2 \rightarrow Co^{2+} + 2OH^{-} \quad (8)$$

$$Co^{2+} + H_2O_2 \rightarrow Co^{3+} + {}^{\bullet}OH + OH^{-} \quad (9)$$

$$Cu^{0} + {}^{\bullet}OH \rightarrow Cu^{+} + OH^{-} \quad (10)$$

$$Cu^{+} + O_2 \rightarrow Cu^{2+} + {}^{\bullet}O_2^{-} \quad (11)$$

$$h^{+} + H_2O + O_2 \rightarrow H^{+} + {}^{\bullet}OH + {}^{\bullet}O_2^{-} \quad (12)$$

$$e^{-} + O_2 \rightarrow {}^{\bullet}O_2^{-} \quad (13)$$

$$2{}^{\bullet}O_2^{-} + 2H^{+} \rightarrow {}^{1}O_2 + H_2O_2 \quad (14)$$

$${}^{\bullet}OH + {}^{\bullet}O_2^{-} \rightarrow {}^{1}O_2 + OH^{-} \quad (15)$$

$$4{}^{\bullet}OH \rightarrow {}^{1}O_2 + 2H_2O \quad (16)$$

$$Co^{3+} + {}^{\bullet}O_2^{-} \rightarrow {}^{1}O_2 + Co^{2+} \quad (17)$$

$$Cu^{2+} + {}^{\bullet}O_2^{-} \rightarrow {}^{1}O_2 + Cu^{+} \quad (18)$$

$$Co^{2+} + Cu^{2+} \rightarrow Co^{3+} + Cu^{+} \quad (19)$$

$${}^{\bullet}O_2^{-} + e^{-} + 2H^{+} \rightarrow H_2O_2 \quad (20)$$

$${}^{\bullet}OH + {}^{\bullet}O_2^{-} + {}^{1}O_2 + h^{+} + e^{-} + \text{phenol} \rightarrow \text{intermediates} + H_2O + CO_2 \quad (21)$$

To systematically investigate the main degradation products of Ph in the $Cu_{0.97}Co_{0.03}$/AC-EB system, UHPLC-QTOF-MS was operated in negative ion electrospray ionization (ESI^{-}) mode. The detailed molecular formulas and structural information of the products are summarized in Table S3, with the corresponding mass spectra presented in Fig. S8 (Supporting information). Based on the identified degradation intermediates and existing research, several potential degradation pathways of Ph under the synergistic action of non-radical and radical processes were proposed, as illustrated in Fig. 5.

In the molecular structure of Ph, all carbon atoms lie in the same plane. The presence of the phenolic hydroxyl group results in an asymmetric electron density distribution on either side of the benzene ring. This leads to preferential accumulation of negative charge at the *ortho*- and *para*-positions relative to the hydroxyl group. Consequently, $^{\bullet}OH$ exhibits selective electrophilic addition at these activated positions, generating hydroquinone and catechol (**M2** and **M3**) [51]. Hydroquinone and catechol can undergo dehydrogenation to form *p*-benzoquinone and *o*-benzoquinone, respectively. Alternatively, they may be further transformed by $^{\bullet}OH$ attack into 1,2,4-benzenetriol and pyrogallol (**M11**, **M12**) [19,52]. Benzoic acid (**M7**) was identified as a degradation product, presumably formed through oxidative carbonylation of Ph to benzaldehyde, followed by further oxidation. The subsequent degradation pathway proceeded through $^{\bullet}OH$-initiated carbon bond cleavage, resulting in aromatic ring opening and the formation of low-molecular-weight

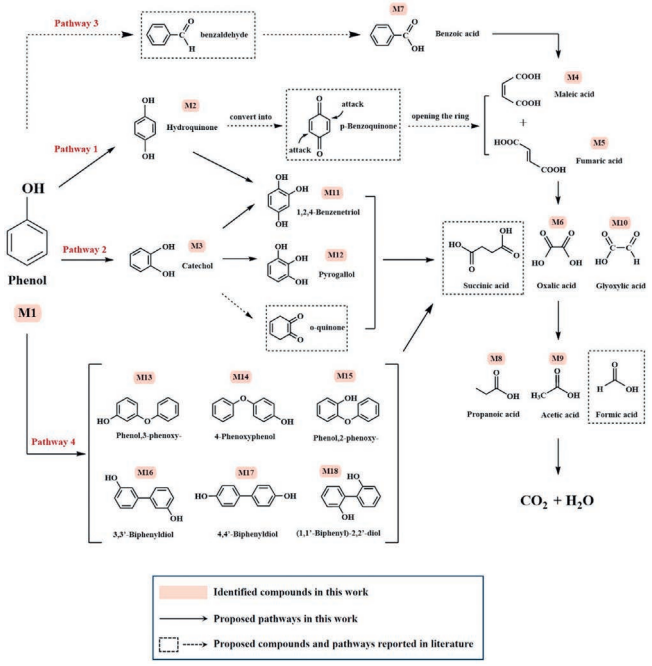


Fig. 5. Proposed degradation pathways of Ph in the $Cu_{0.97}Co_{0.03}$/AC-EB system.

unsaturated acids, such as maleic acid (**M4**) [14]. Under acidic conditions (H^{+}), maleic acid underwent isomerization to form its trans-isomer, fumaric acid (**M5**). These dicarboxylic acids subsequently underwent further oxidative degradation to yield oxalic acid (**M6**), glyoxylic acid (**M10**), propionic acid (**M8**), and acetic acid (**M9**) [19,53]. Ultimately, partial intermediate products were completely mineralized into CO_2 and H_2O.

Furthermore, under $^{1}O_2$ attack, the benzene ring of phenol readily forms unstable hydroxycyclohexadienyl intermediates, which reveals an alternative degradation pathway. In this process, both $^{\bullet}OH$ and $^{\bullet}O_2^{-}$ radicals participate cooperatively in phenol dehydrogenation, generating phenoxyl radicals. These radicals subsequently undergo copper-catalyzed coupling with hydroxycyclohexadienyl intermediates to yield hydroxylated biphenyl products (**M13**-**M15**). Simultaneously, the hydroxycyclohexadienyl intermediates can undergo mutual coupling to generate a series of dihydroxybiphenyl isomers (**M16**-**M18**), which ultimately undergo oxidative ring cleavage for complete mineralization [54].

Toxicity evaluation of Ph and its degradation intermediates was performed using T.E.S.T. (version 5.1.2) based on the quantitative structure-activity relationship (QSAR) method [55–57]. The evaluation included six parameters: Fathead minnow 50% lethal concentration in 96 h (LC_{50}–96 h), Daphnia magna 50% lethal concentration in 48 h (LC_{50}–48 h), Oral rat 50% lethal dose (LD_{50}), Developmental toxicity, Bioconcentration factor (BCF), and Ames mutagenicity. The prediction results are presented in Fig. 6 and Table S4 (Supporting information).

The LC_{50}–96 h value was 38.69 mg/L for Ph, which can be categorized as "Harmful" (Fig. 6a). Most degradation intermediates exhibited lower LC_{50} values than Ph, indicating a significant reduction in toxicity. The LD_{50} value of Ph was 434.02 mg/kg, which was classified as "Toxic" (Fig. 6b). Similarly, most of the intermediates (except M3 and M8) demonstrated lower toxicity compared to Ph. Meanwhile, the LC_{50}–48 h value of Ph was 7.44 mg/L, which was considered "Toxic", while several intermediates turned to "Harmful" or "Not harmful" (except **M13**-**M18**), as shown in Fig. 6c. Nevertheless, the radiolytic catalytic degradation process reduced the developmental toxicity of most intermediates rela-

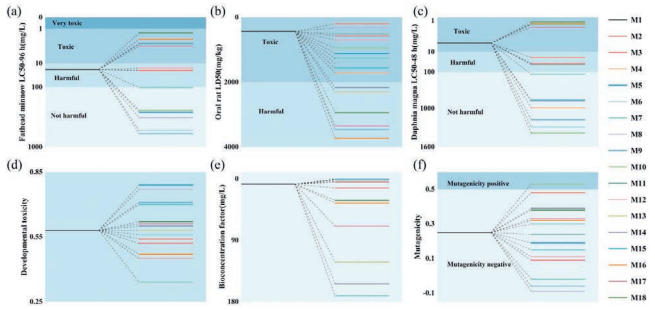


Fig. 6. Toxicity assessment of Ph and its degradation intermediates. (a) Fathead minnow 50% lethal concentration in 96 h (LC_{50}–96 h). (b) Oral rat 50% lethal dose (LD_{50}). (c) Daphnia magna 50% lethal concentration in 48 h (LC_{50}–48 h). (d) Developmental toxicity. (e) Bioconcentration factor (BCF), and (f) mutagenicity.

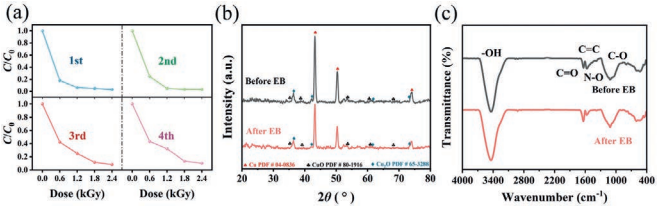


Fig. 7. Stability evaluation of $Cu_{0.97}Co_{0.03}$/AC catalyst under EB irradiation. (a) Cyclic Ph removal efficiency, (b) XRD patterns and (c) FTIR spectra of $Cu_{0.97}Co_{0.03}$/AC before and after EB irradiation.

tive to Ph (Fig. 6d). The BCF values of most intermediates were higher than that of Ph. BCF reflects environmental accumulation potential rather than direct toxicity. High BCF values indicate efficient chemical transfer from aquatic environments into organisms. Consequently, compounds may exhibit low acute toxicity despite high internal concentrations, requiring extreme body burdens to elicit lethal effects. Such "inert accumulation" does not denote safety: Sustained high concentrations may induce chronic toxicity through prolonged biological residence, including reproductive impairment, developmental abnormalities, and endocrine disruption. For the mutagenicity toxicity (Fig. 6f), more than half of the degradation intermediates exhibited lower mutagenicity with negative predicted results (except **M10**). These results demonstrate that the $Cu_{0.97}Co_{0.03}$/AC-EB system effectively reduced the toxicity of Ph and its intermediates.

Fig. 7a displays the residual Ph concentrations across multiple cycles, demonstrating nearly complete Ph removal within 1.2 kGy during the first two cycles with minimal reaction rate variation. After four cycles, the system still maintained 90.0% total Ph removal efficiency at 2.4 kGy. The observed activity reduction may be attributed to both partial leaching of doped metal ions and active site occlusion by adsorbed organic intermediates [55]. XRD and FTIR analyses revealed no significant structural changes in $Cu_{0.97}Co_{0.03}$/AC before and after reaction (Figs. 7b and c). These results collectively demonstrated that $Cu_{0.97}Co_{0.03}$/AC still maintained a high catalytic efficiency and excellent stability during cyclic operation.

In conclusion, the $Cu_{0.97}Co_{0.03}$/AC bimetallic catalyst prepared *via* the impregnation method demonstrated outstanding Ph degradation and mineralization under EB irradiation. EB irradiation directly cleaved water molecules to generate reactive radicals (*e.g.*, $^{\bullet}OH$) for primary Ph degradation, while radiolytically produced H_2O_2 was activated by Cu/Co species. This synergy established a dual reaction network comprising both radical ($^{\bullet}OH$, $^{\bullet}O_2^-$) and non-radical ($^1O_2$, h^+, e^-) pathways, achieving 6.92-fold and 41.43-fold enhancements in Ph degradation and TOC removal, respectively, compared with EB irradiation alone. Quenching experiments and EPR analyses identified $^{\bullet}OH$ and $^1O_2$ as the dominant reactive species, with $^{\bullet}O_2^-$ serving as a crucial intermediate for both H_2O_2 production and $^1O_2$ formation. Compared to conventional advanced oxidation processes, this EB-catalysis synergy system achieves exceptional efficacy of high efficiency and environmental compatibility, providing a novel solution for recalcitrant organic pollutant treatment.

CRediT authorship contribution statement

Yalan Deng: Writing – original draft, Investigation. **Yaqi Wu:** Validation, Resources, Data curation. **Haipeng Xiao:** Resources, Formal analysis. **Nuowen Ma:** Software, Methodology. **Huifang Miao:** Supervision, Conceptualization. **Liuxuan Cao:** Writing – review & editing, Supervision, Methodology, Funding acquisition, Conceptualization. **Wei Guo:** Methodology, Conceptualization.

Declaration of competing interest

The authors declare that they have no known competing financial interests or personal relationships that could have appeared to influence the work reported in this paper.

Acknowledgments

This work was supported by the National Natural Science Foundation of China (No. 12175188), Nuclear energy development and research projects (No. HNKF202228(30)), XMU Training Program of Innovation and Entrepreneurship for Undergraduates (No. 2021X1173).

Supplementary materials

Supplementary material associated with this article can be found, in the online version, at doi:10.1016/j.cclet.2025.111568.

References

[1] P. Ding, P. Wu, Q. Cao, et al., Sci. Total. Environ. 901 (2023) 166342.
[2] Z. Peng-sheng, G. Zhong-quan, X. Yan, in: IOP Conf. Ser. Earth Environ. Sci., 546, 2020, 042037.
[3] S. Li, J. Xie, J. Gu, M. Zhou, Chin. Chem. Lett. 34 (2023) 108204.
[4] R. Huang, T. Feng, S. Wu, et al., Environ. Res. 234 (2023) 116604.
[5] F.Z. Yehia, G. Eshaq, A.M. Rabie, et al., Egypt. J. Pet. 24 (2015) 13–18.
[6] X. Wei, H. Wu, G. He, Y. Guan, J. Hazard. Mater. 321 (2017) 408–416.
[7] H.-X. Zou, Y.-Y. Xu, X. Fan, et al., J. Water Process. Eng. 64 (2024) 105542.
[8] F. Li, Q. Luo, W. Zhen, et al., Water, Air, Soil Pollut 235 (2024) 371.
[9] Y.M. Dong, G.L. Wang, P.P. Jiang, et al., Chin. Chem. Lett. 22 (2011) 209–212.
[10] F. Yang, S.Q. Yang, X. Zhong, et al., Rare Met. 43 (2024) 1869–1882.
[11] W.L. Tu, G. Wang, Y. Zhang, et al., Rare Met. 43 (2024) 3146–3160.
[12] L. Shi, X. Zou, T. Wang, et al., Chin. Chem. Lett. 33 (2022) 442–446.
[13] J. Li, Z. Zhao, Z. Li, et al., Chin. Chem. Lett. 33 (2022) 3705–3708.
[14] H. Xu, X. Sun, H. Yang, et al., J. Cleaner Prod. 436 (2024) 140672.
[15] H. Yu, D. Liu, H. Wang, et al., Chin. J. Catal. 43 (2022) 2678–2689.
[16] J. Wang, R. Zhuan, Sci. Total Environ. 701 (2020) 135023.
[17] F.K. Tominaga, A.P. dos Santos Batista, A.C. Silva Costa Teixeira, S.I. Borrely, J. Environ. Chem. Eng. 6 (2018) 4605–4611.
[18] N. Chitose, S. Ueta, S. Seino, T.A. Yamamoto, Chemosphere 50 (2003) 1007–1013.
[19] T.S. Alkhuraiji, S.O.B. Boukari, F.S. Alfadhl, J. Hazard. Mater. 328 (2017) 29–36.
[20] Y. Lei, Y. Zhou, S. Zhang, et al., Sep. Purif. Technol. 326 (2023) 124785.
[21] R. Zhang, Z.X. Zhang, F. Wang, D. Chen, J. Taiwan. Inst. Chem. Eng. 145 (2023) 104815.
[22] J. Qu, W. Tong, J. Zhang, et al., J. Cleaner Prod. 419 (2023) 138216.
[23] Z. Pan, X. Qian, New Carbon Mater. 37 (2022) 180–195.
[24] C. Wang, H. Dai, L. Liang, et al., J. Hazard. Mater. 458 (2023) 132002.
[25] M. Xi, K. Cui, M. Cui, et al., Chem. Eng. J. 420 (2021) 129902.
[26] P. Hong, K. Zhang, J. He, et al., J. Hazard. Mater. 435 (2022) 128958.
[27] L. Chu, S. Zhuang, J. Wang, Radiat. Phys. Chem. 145 (2018) 34–38.
[28] A. Toprak, Biomass Convers. Biorefin. 10 (2019) 977–986.
[29] A. El Nemr, R.M. Aboughaly, A. El Sikaily, et al., Biomass Convers. Biorefin. 13 (2021) 1613–1631.
[30] M. Wang, H. Chen, M. Wang, et al., Angew. Chem. Int. Ed. 62 (2023) e202306456.
[31] H. Wang, J. Zhang, P. Wang, et al., Chin. Chem. Lett. 31 (2020) 2789–2794.

[32] J. Singh, J.K. Yang, Y.Y. Chang, J. Environ. Manage. 175 (2016) 60–66.
[33] L. Kemmou, Z. Frontistis, J. Vakros, et al., Catal. Today 313 (2018) 128–133.
[34] G. Nagaraju, G.S.R. Raju, Y.H. Ko, J.S. Yu, Nanoscale 8 (2016) 812–825.
[35] J. Zheng, Q. Lin, Y. Liu, et al., Chem. Eng. J. 452 (2023) 139233.
[36] M. Gao, Z. Wang, Z. Liu, et al., Adv. Mater. 35 (2023) 2305575.
[37] I. Khalakhan, M. Vorokhta, X. Xie, et al., J. Electron Spectrosc. Relat. Phenom. 246 (2021) 147027.
[38] I. Platzman, R. Brener, H. Haick, R. Tannenbaum, J. Phys. Chem. C 112 (2008) 1101–1108.
[39] G. Han, X. Zhang, W. Liu, et al., Nat. Commun. 12 (2021) 6335.
[40] Y. Yang, R. Zeng, Y. Xiong, et al., J. Am. Chem. Soc. 141 (2019) 19241–19245.
[41] H. Zhu, R. Du, H. Zhao, et al., J. Mater. Chem. A 12 (2024) 8487–8501.
[42] S. Xiong, J. Chen, N. Huang, et al., Environ. Sci. Technol. 53 (2019) 10379–10386.
[43] J. He, Q. Ye, Y. Zhu, et al., Radiat. Phys. Chem. 208 (2023) 110958.
[44] J. Wang, X. Guo, J. Hazard. Mater. 390 (2020) 122156.
[45] L. Largitte, R. Pasquier, Chem. Eng. Res. Des. 109 (2016) 495–504.
[46] Y. Chen, C. Fan, X. Li, et al., J. Chem. Technol. Biotechnol. 98 (2022) 117–128.
[47] S. Zhang, J. Kuang, K. Wei, et al., Colloids Surf. A 677 (2023) 132384.
[48] Y. Liu, H. Zhou, C. Jin, et al., Appl. Catal. B 338 (2023) 123061.
[49] Y. Wu, C. Song, X. Yu, et al., Chem. Eng. J. 480 (2024) 147984.
[50] W. Zhang, L. Wang, C. Hou, et al., Environ. Sci.: Nano 11 (2024) 2481–2493.
[51] J. Morales-Roque, M. Carrillo-Cárdenas, N. Jayanthi, et al., J. Mol. Struct.:Theochem. 910 (2009) 74–79.
[52] T.T.T. Dang, S.T.T. Le, D. Channei, et al., Res. Chem. Intermed. 42 (2016) 5961–5974.
[53] S. Wang, J. Hu, S. He, J. Wang, J. Hazard. Mater. 433 (2022) 128727.
[54] X. Li, Y. Yang, H. Li, J. Ma, Water Sci. Technol. 2017 (2018) 340–350.
[55] X. Liu, J. Zhou, D. Liu, S. Liu, Sep. Purif. Technol. 306 (2023) 122526.
[56] J. Wei, J. Bi, L. Zhang, et al., Sep. Purif. Technol. 280 (2022) 119975.
[57] X.H. Yi, H. Ji, C.C. Wang, et al., Appl. Catal. B 293 (2021) 120229.